JACS
JOURNAL OF THE AMERICAN CHEMICAL SOCIETY

ARTICLE

pubs.acs.org/JACS

Structure Sensitivity of Alkynol Hydrogenation on Shape- and Size-Controlled Palladium Nanocrystals: Which Sites Are Most Active and Selective?

Micaela Crespo-Quesada,[†] Artur Yarulin,[†] Mingshang Jin,[‡] Younan Xia,[‡] and Lioubov Kiwi-Minsker*[,†]

[†]Group of Catalytic Reaction Engineering, Ecole Polytechnique Fédérale de Lausanne, 1015 Lausanne, Switzerland

[‡]Department of Biomedical Engineering, Washington University, Saint Louis, Missouri 63130, United States

Supporting Information

ABSTRACT: The activity and selectivity of structure-sensitive reactions are strongly correlated with the shape and size of the nanocrystals present in a catalyst. This correlation can be exploited for *rational catalyst design*, especially if each type of surface atom displays a different behavior, to attain the highest activity and selectivity. In this work, uniform Pd nanocrystals with cubic (in two different sizes), octahedral, and cuboctahedral shapes were synthesized through a solution-phase method with poly(vinyl pyrrolidone) (PVP) serving as a stabilizer and then tested in the hydrogenation of 2-methyl-3-butyn-2-ol (MBY). The observed activity and selectivity suggested that two types of active sites were involved in the catalysis—those on the planes and at edges—which differ in their coordination numbers. Specifically, semihydrogenation of MBY to 2-methyl-3-buten-2-ol (MBE) occurred preferentially at the plane sites regardless of their crystallographic orientation, $Pd_{(111)}$ and/or $Pd_{(100)}$, whereas overhydrogenation occurred mainly at the edge sites. The experimental data can be fit with a kinetic modeling based on a two-site Langmuir−Hinshelwood mechanism. By considering surface statistics for nanocrystals with different shapes and sizes, the optimal catalyst in terms of productivity of the target product MBE was predicted to be cubes of roughly 3−5 nm in edge length. This study is an attempt to close the material and pressure gaps between model single-crystal surfaces tested under ultra-high-vacuum conditions and real catalytic systems, providing a powerful tool for rational catalyst design.

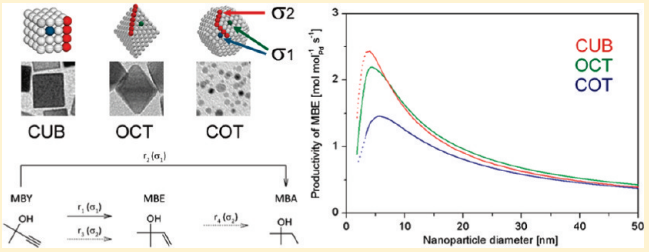

INTRODUCTION

The structure sensitivity of reactions catalyzed by metal nanocrystals has attracted considerable attention over the past decades.[1] The activity and selectivity of structure-sensitive reactions are strongly affected by both the size and shape of the nanocrystals in a catalyst. The ratio between surface atom types (e.g., vertex, edge, and plane) changes substantially when varying the size of a nanocrystal (Figure S1, Supporting Information). The fraction of atoms located on (111) and/or (100) crystallographic planes increases with size at the expense of edge and vertex atoms. This change leads to a *size effect*, which manifests itself with an increase (antipathetic structure sensitivity) or decrease (sympathetic structure sensitivity) of the turnover frequency (TOF) as a function of particle size.[2] In addition, shape variation can result in important morphological differences: for example, cubes display only (100) plane atoms on the surface, while octahedra present only (111) plane atoms, and cuboctahedra have a mixture of both.[3,4] This difference contributes to a *shape effect*, especially when each type of surface atom possesses a different reactivity. For structure-sensitive reactions, such shape and size effects could be used to perform a *rational catalyst design* to achieve a superior catalyst in terms of activity and/or selectivity.

Many recent studies have been carried out to investigate the catalytic behaviors of different crystal planes on model catalysts.[5−7] Most of these studies were performed in ultrahigh vacuum using single metal crystals exhibiting definite crystallographic planes. However, these model catalysts are far away from the real catalytic systems. These *material and pressure gaps* are believed to be overcome using stable nanostructures with desirable crystallographic orientations such as nanowires,[8] cubes,[9] tetrahedra,[10,11] and cuboctahedra.[12,13] Indeed, synthesis of nanocrystals with different shapes has been achieved through colloidal methods for a wide variety of different metals.[14−16] These nanocrystals with well-defined shapes can be used as prepared as catalysts to explore the facet sensitivity of liquid-phase reactions. Recent reviews gather the results of the catalytic behavior of colloidal nanocrystals in cross-coupling, electron transfer, hydrogenation, and oxidation reactions.[14,17]

Among structure-sensitive reactions, Pd-catalyzed alkyne hydrogenations are of special interest due to their importance in bulk and fine chemical production. The size effect for this type of reaction was first reported by Boitiaux and co-workers.[18]

Received: May 18, 2011
Published: July 13, 2011

Recently, it was shown that the dependence of TOF on the particle size disappeared when only one type of surface atom, namely, $Pd_{(111)}$, was taken into account,[19,20] suggesting that these atoms were the active sites involved in the catalysis. Using this approach, atoms located on $Pd_{(111)}$ have been identified as the active sites in the hydrogenation of 1,3-butadiene[6,7] and 2-methyl-3-butyn-2-ol (MBY).[21,22] However, the nanocrystals used in these size-dependence studies presented only a very low percentage of $Pd_{(100)}$ atoms on the surface,[6,7,21−24] implying that their influence, although measurable, might be easily overlooked. Furthermore, the existence of two or more different kinds of active sites responsible for observed size effects has not been thoroughly discussed in the literature.[25]

In this work, poly(vinyl pyrrolidone) (PVP)-stabilized Pd nanocrystals with well-defined shapes were synthesized and tested *per se* (without any catalytic support) in the water-assisted selective hydrogenation of MBY in order to compare the activity and selectivity of plane surface atoms, namely, $Pd_{(100)}$ and $Pd_{(111)}$, with edge surface atoms, Pd_{edge}. Specifically, we examined Pd nanocubes of two different sizes (6 and 18 nm in edge length), Pd octahedra of 31 nm in edge length, and Pd cuboctahedra of 5.5 nm in size. A simple model involving two different types of active sites, Pd_{plane} and Pd_{edge}, was used to successfully describe the differences observed in activity and selectivity between the samples. The kinetic modeling was performed using a two-site Langmuir−Hinshelwood mechanism, with one single set of kinetic and adsorption constants specific to the reaction path or adsorption equilibrium of a compound on a given active site. The results of modeling were consistent with our observations, which, in turn, allowed optimizing the Pd catalyst's size and shape.

METHODS

Nanocrystal Synthesis. Both the Pd nanocubes and cuboctahedra were synthesized according to our previously published protocols.[26,27] For the Pd octahedra, they were prepared as follows: 3 mL of an aqueous Na_2PdCl_4 solution (9.5 mg/mL) was added into an aqueous solution (8 mL) containing 105 mg of PVP, 100 μL of CH_3CHO, and 0.3 mL of the Pd nanocubes (1.8 mg/mL, 18 nm in edge length) and was stirred at 60 °C for 3h, after which it was allowed to cool down to room temperature. The final products were collected by centrifugation and washed with ethanol and water to remove excess PVP.

Characterization. The shape and size of the nanocrystals were analyzed by transmission electron microscopy (TEM), using a Philips CM20 microscope operated at 200 kV. High-resolution TEM images were recorded with a CM300 FEG (Philips/FEI) microscope operated at 300 kV.

To determine the amount of Pd loaded in each catalytic run, an aliquot of the nanocrystal suspension was analyzed by atomic absorption spectroscopy using a Shimadzu AA-6650 spectrometer. The specific wavelength used for Pd^{2+} was 475 nm.

X-ray photoelectron spectroscopy (XPS) data were collected using an Axis Ultra instrument (Kratos Analytical, Manchester, UK) under ultra-high-vacuum condition ($<10^{-8}$ Torr) and with a monochromatic Al Kα X-ray source (1486.6 eV). The adventitious carbon 1s peak was calibrated at 284.5 eV and used as an internal standard to compensate for any charging effects.

Hydrogenation Reactions. The reactions were carried out in a baffled semibatch stainless steel reactor (250 mL autoclave, Büchi AG, Switzerland) equipped with a heating jacket and a hydrogen supply system. An eight-blade disk turbine impeller was used as the stirrer. The molar ratio between MBY and surface Pd atoms was kept at a constant ~140 000 in all cases. An appropriate amount of the Pd nanocrystals and 1 g of MBY were diluted with water up to 200 mL and sonicated for 5 min before introducing them into the reactor. After the reactor had been charged, it was flushed with N_2 and set to 60 °C. Subsequently, it was flushed with H_2 and pressurized to 0.3 MPa. Samples were periodically withdrawn from the reactor and analyzed by gas chromatography. The accuracy of the analysis was found to be 0.1 wt % for all products.

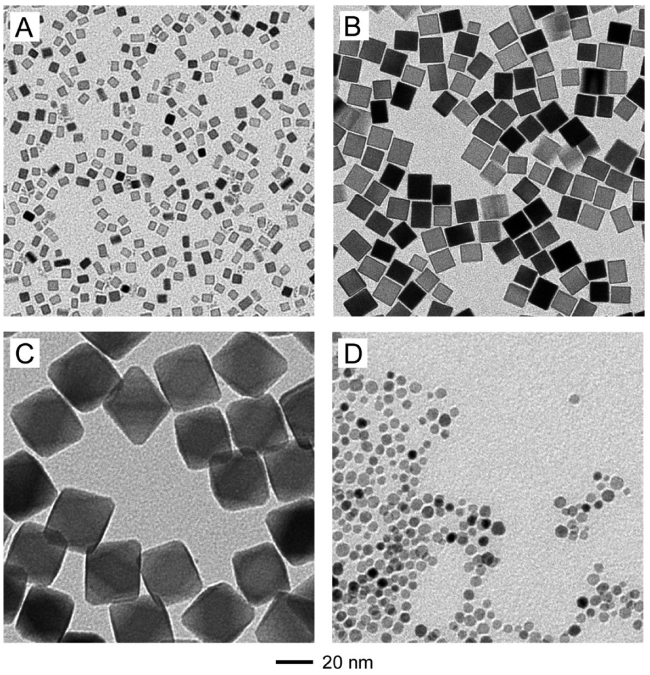

Figure 1. TEM images of the PVP-stabilized Pd nanocrystals used in this work: (A) 6 nm cubes, (B) 18 nm cubes, (C) 31 nm octahedra, and (D) 5.5 nm cuboctahedra.

RESULTS AND DISCUSSION

Synthesis and Characterization of the Pd Nanocrystals with Controlled Shapes and Sizes. We synthesized Pd nanocubes, octahedra, and cuboctahedra to investigate the effect of shape on catalytic properties. We also prepared Pd nanocubes with two different sizes using a bromide-assisted method described previously (Figure 1A and B).[27] Figure 1 shows TEM images of the Pd nanocrystals, where the Pd octahedra were obtained by reducing a Pd precursor with CH_3CHO in the presence of the 18 nm Pd nanocubes as seeds (Figure 1C), and the Pd cuboctahedra were synthesized by reducing a Pd precursor with L-ascorbic acid in the presence of PVP (Figure 1D). HRTEM imaging of each sample showed the nanocrystals to be monocrystalline and bounded by the expected crystallographic planes as seen in Figure S2 in the Supporting Information. Furthermore, particle counting allowed determining the average particle size of each sample in which more than 95% of the nanocrystals corresponded to the expected shapes (Figure S3, Supporting Information).

Despite the extensive cleaning procedures to which the nanocrystals are subjected, it is common to find traces of the stabilizing agent in the samples, which can modify the behavior of the catalyst.[13,28,29] Therefore, during this study, all samples were prepared with the same stabilizer, namely, PVP. Furthermore, XPS analyses did not detect Br^- or Cl^- on the surface of the nanocrystals after cleaning, as shown in Figure S4 of the

Table 1. Statistics of Surface Atoms[4] for the Nanocrystals Used in This Work

		surface statistics			
sample	d_p [nm]	D^a [%]	$x_{111}{}^b$ [%]	$x_{100}{}^b$ [%]	$x_{edge}{}^b$ [%]
CUB6	6	16.7		72.1	15.8
CUB18	18	6.0		90.0	6.0
OCT	31	3.6	93.2		5.5
COT	5.5	18.3	43.7	5.6	30.3

[a] Dispersion (%), defined as the ratio of the number of surface atoms (N_S) to the total number of atoms (N_T). [b] Fraction of surface atoms of a given type, $x_i = N_i/N_S$

Scheme 1. General Reaction Network for the Hydrogenation of 2-Methyl-3-butyn-2-ol (MBY)

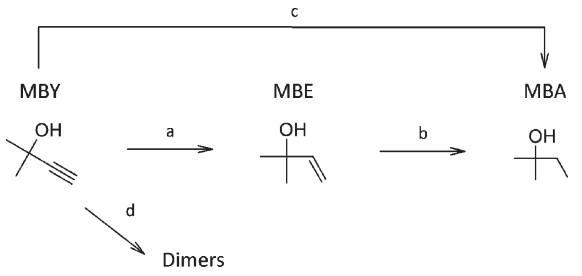

Supporting Information for CUB6. The XPS spectra of the other samples were analogous to the former.

The statistics of surface atoms[4] for ideal face-centered cubic (fcc) nanocrystals allow one to determine the relative numbers of different types of surface atoms on a nanocrystal with a particular size and shape (see Figure S1, Supporting Information). Concern has been expressed regarding the utilization of idealistic models to characterize the surface of nanocrystals.[25] Therefore, a non-ideal model was employed in the present work,[4] where an incomplete extra layer of atoms was added to the surface of the nanocrystal. Table 1 summarizes this information for the Pd nanocrystals used in this work. TEM imaging was used to obtain the mean particle diameter.

Structure Sensitivity of MBY Hydrogenation. The reaction network for MBY hydrogenation is depicted in Scheme 1.[21,22,30,31] MBY can be either semihydrogenated to 2-methyl-3-buten-2-ol (MBE) through path a, directly hydrogenated to 2-methyl-3-butan-2-ol (MBA) through path c, or oligomerized into C-10 species through path d. Furthermore, MBE can be overhydrogenated to MBA through path b. In this work path d was not observed and was thus eliminated from the network for simplicity. In our previous study,[22] the hydrogenation of MBY showed an antipathetic structure sensitivity, suggesting at first glance that only plane surface atoms were responsible for the catalytic activity of Pd nanocrystals, since their relative amount increases with particle size (see Figure S1, Supporting Information).

The Pd nanocrystals shown in Figure 1 were tested as unsupported catalysts for the water-assisted hydrogenation of MBY. In order to confirm the morphological stability of the catalysts during the reaction, cubic nanocrystals were subjected to the reaction conditions for 2.5 h and were observed with TEM immediately after. The nanocrystals maintained their shape (Figure S5, Supporting Information), and, being the least favorable shape, the result could be extrapolated to the other nanocrystals.

All nanocrystals were active, thus confirming that $Pd_{(100)}$ present on cubes could indeed catalyze the hydrogenation of MBY. The values for MBY transformation rate and TOF are summarized in Table 2. In order to evaluate the specific activities of the various types of surface atoms, two models describing the observed TOF were applied. The first activity model (A) is based on the assumption that the observed activity (TOF_{obs}) depends linearly on the fraction of each plane atom (x_i) and their specific activity (TOF_i):

$$\text{A}: \mathrm{TOF_{obs}} = \mathrm{TOF_{111}}x_{111} + \mathrm{TOF_{100}}x_{100} \quad (1)$$

Edge atoms were considered to be inactive, following the results published in the literature.[6,7,19−22] As a result, the observed *size and/or shape dependence* of the nanocrystals would actually be due to the change of the relative amount of surface atoms.

Model A was first applied to CUB18 and OCT, the two samples with the highest fraction of plane atoms. Equation 1, together with the statistics of surface atoms from Table 1, was used to estimate TOF_{111} and TOF_{100}. From these calculations, $Pd_{(100)}$ and $Pd_{(111)}$ plane atoms were found to be almost equally active in MBY hydrogenation. The model was, however, unable to predict the observed values of TOF for CUB6 and COT. These results, together with the fact that CUB6 and COT samples present 15% and 30% of low-coordination (edge) atoms on their surfaces, suggest that a model including the latter would be able to describe the system more accurately. Since $Pd_{(100)}$ and $Pd_{(111)}$ plane atoms were found to show a similar activity, model B was suggested as follows:

$$\text{B}: \mathrm{TOF_{obs}} = \mathrm{TOF_{plane}}x_{plane} + \mathrm{TOF_{edge}}x_{edge} \quad (2)$$

The application of model B (see Table 2) simultaneously to all four samples allowed the estimation of the specific plane and edge TOFs, which were found to be 19.3 ± 2.4 and 4.7 ± 0.8 s^{-1}, respectively. This result suggests that MBY adsorbs on all types of surface atoms, but its reactivity depends on the coordination number of the active site. Indeed, strong adsorption strengths of the electron-rich alkyne on low-coordination atoms, such as edge atoms, led to a decrease in activity in the hydrogenation of 1-butyne.[32,33] It is worth noting that model B can account for the antipathetic structure sensitivity shown in MBY hydrogenation, since an increase in size will still imply an increase in TOF_{obs}.

Selectivity toward the target product, MBE, also pointed toward the existence of two types of active sites, namely, plane and edge atoms. Figure 2 shows the selectivity at 50% and 95% conversion of each sample as a function of the fraction of edge atoms on their surfaces. It can be appreciated that at 50% conversion selectivity is independent of both the size and shape of the nanocrystal. This is in line with the thermodynamic selectivity shown in alkyne hydrogenations: as long as the coverage of the alkyne is high enough, it will "block" the active sites due to its higher adsorption strength as compared to the olefinic compound.[3] This observation implies that both the plane and edge sites selectively semihydrogenate toward MBE, only that the rate over the latter is 4-fold lower than the rate over the former.

Table 2. Activity[a] Models A and B As Applied to the Catalytic Responses of Differently Shaped Pd Nanocrystals to Account for the Structure Sensitivity of the Reaction

			model A[b]			model B[c]	
sample	$-R_{MBY}$ [mol·mol$_{Pd}^{-1}$·s^{-1}]	TOF$_{obs}$ [s^{-1}]	TOF$_{111}$ [s^{-1}]	TOF$_{100}$ [s^{-1}]	TOF$_{est}$ [s^{-1}]	TOF$_{plane}$ [s^{-1}]	TOF$_{edge}$ [s^{-1}]
CUB6	2.55	15.3		19.2	13.8	19.3 ± 2.4	4.7 ± 0.8
CUB18	1.05	17.5		19.2	17.5		
OCT	0.53	14.6	15.6		14.6		
COT	2.25	12.3	15.6	19.2	9.3		

[a] Reaction conditions: 1 g of MBY, MBY:Pd$_{surf}$ = 140 000, 200 mL of H_2O, 60 °C, 0.3 MPa of H_2. [b] In this model, TOF$_{111}$ and TOF$_{100}$ were first estimated from OCT and CUB18, respectively, and then applied to CUB6 and COT samples. [c] All samples were fitted simultaneously.

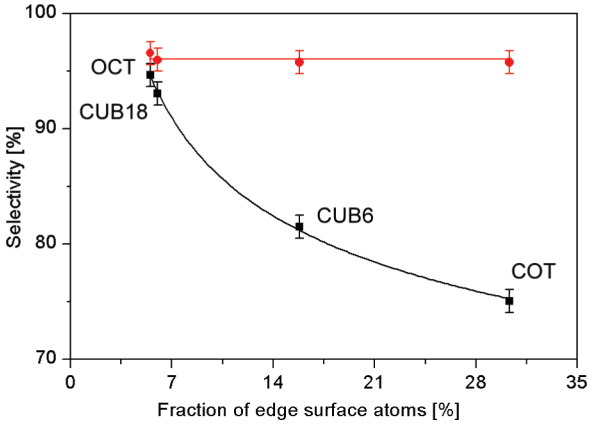

Figure 2. Selectivity toward the target product, 2-methyl-3-buten-2-ol (MBE), at 50% (●) and 95% (■) conversion of MBY as a function of the amount of edge atoms.

When approaching full conversion, however, there seems to be a clear correlation between overhydrogenation and the amount of edge atoms (Figure 2). For a given metal, the adsorption strength of the substrate varies in the same order: aromatic < olefin < diolefin < alkyne. A plot depicting the activity of the metal as a function of the adsorption strength thus gives rise to the known "volcano" curve with the maximum located between olefins and diolefins.[33] This observation implies that an increase in the adsorption strength of the alkyne, such as adsorbing on an edge atom rather than on a plane atom, would reduce the activity, whereas an opposite trend would be observed for the olefin. Therefore, at high conversion, when the coverage of MBY becomes insufficient to ensure the blocking of all active sites, MBE can adsorb and overhydrogenate toward MBA. The rate for overhydrogenation of MBE should then be higher on edge sites than on plane sites. This was indeed observed at 95% conversion on CUB18 and OCT samples, which contained very few edge sites and demonstrated the lowest selectivity to MBA. These results are in line with the literature, where at high dispersions, i.e., small particle size, 1-butene hydrogenation was fast, whereas hydrogenation of 1-butyne decreased sharply.[32] Furthermore, the edge sites were recently suggested as possible active sites for the hydrogenation of MBE to MBA over Pd.[34]

Figure 3 shows schematically the active sites present on each type of nanocrystal used in this work, where Pd$_{(111)}$ and Pd$_{(100)}$ plane atoms were considered as a single site (σ_1) and edge atoms were considered as another type of active site (σ_2). The reaction network for MBY hydrogenation shown in Scheme 1 can then be modified to include the observations gathered experimentally

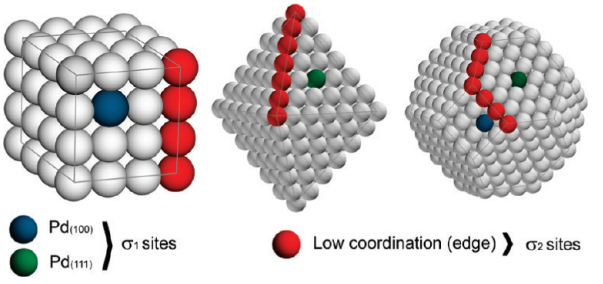

Figure 3. Schematic illustrations of the two types of active sites involved in the hydrogenation of MBY. Atoms on the planes, regardless of their crystallographic orientations, constitute the first type of active site, σ_1. Low-coordination atoms, or atoms at the edges, represent the second type of active site, σ_2.

Scheme 2. Modified Reaction Network for the Hydrogenation of MBY, Showing the Active Sites Involved in Each Path

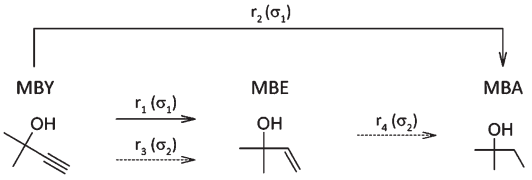

Table 3. Set of Constants Used to Model All Samples Simultaneously[a]

adsorption constants [L mol^{-1}]				kinetic constants [mol mol$^{-1}_{surf\ Pd}$ s^{-1}]			
$K_{Y,\sigma1}$	$K_{Y,\sigma2}$	$K_{E,\sigma1}$	$K_{E,\sigma2}$	$k^{***}_{1,\sigma1}$	$k^{***}_{2,\sigma1}$	$k^{***}_{3,\sigma2}$	$k^{***}_{4,\sigma2}$
20.5	56.5	0.2	2.7	83.8	2.3	24.0	428.2

[a] Reaction conditions: 1 g of MBY, MBY:Pd$_{surf}$ = 140 000, 200 mL of H_2O, 60 °C, 0.3 MPa of H_2.

(see Scheme 2). The semihydrogenation of MBY proceeds through both σ_1 and σ_2 sites. The direct hydrogenation of MBY to MBA, observed even at low conversion, takes place exclusively on σ_1 sites. The overhydrogenation of MBE to MBA, on the other hand, is catalyzed solely by σ_2 sites. Equation 2 can now be rewritten as

$$\mathrm{TOF}_{obs} = \mathrm{TOF}_{\sigma_1} x_{\sigma_1} + \mathrm{TOF}_{\sigma_2} x_{\sigma_2} \quad (3)$$

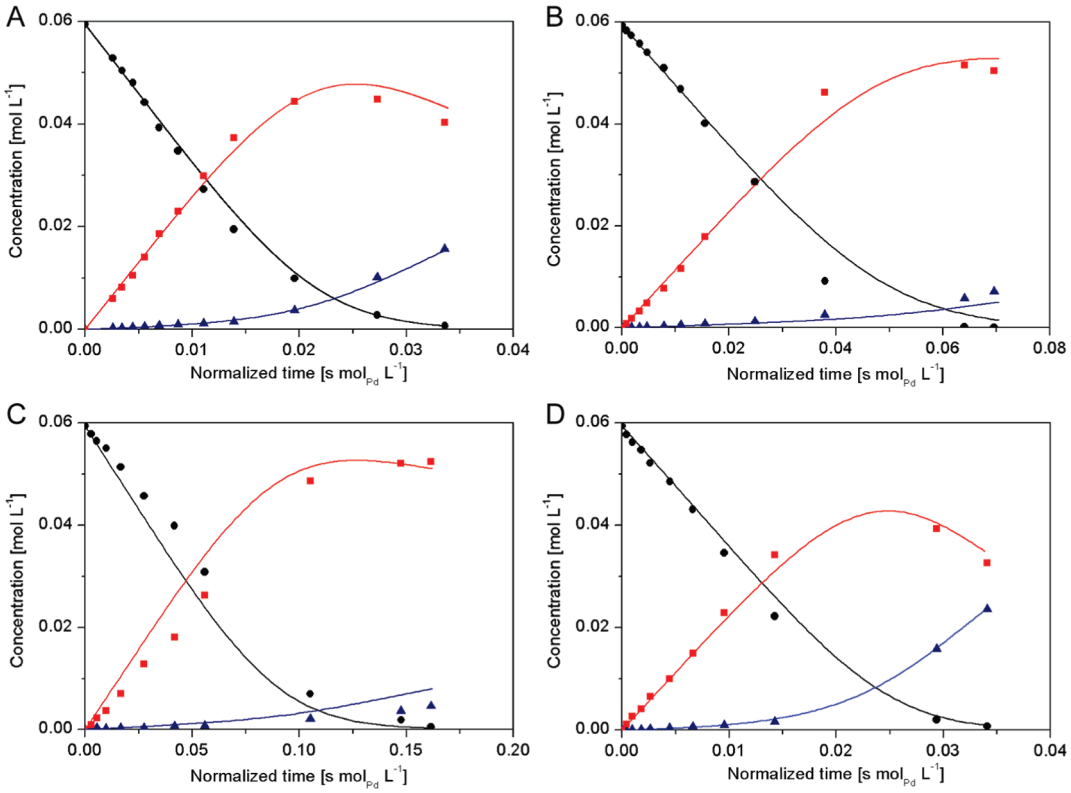

Figure 4. Experimental data points for 2-methyl-3-butyn-2-ol (MBY, ●), 2-methyl-3-buten-2-ol (MBE, ■), and 2-methyl-3-butan-2-ol (MBA, ▲) and the prediction curves obtained with a single set of adsorption and kinetic constants for (A) CUB6, (B) CUB18, (C) OCT, and (D) COT samples. Reaction conditions: 1 g of MBY, MBY:Pd_{surf} = 140 000, 200 mL of H_2O, 60 °C, 0.3 MPa of H_2.

Kinetic Modeling. In order to model the reaction kinetics, a Langmuir−Hinshelwood mechanism assuming two types of active sites as well as dissociative hydrogen adsorption[35] and bimolecular reactions between the adsorbed species was applied. The detailed derivation of the reaction rate expressions can be found in the Supporting Information. The full kinetic expressions obtained are shown below:

$$r_1 = \frac{k_{1,\sigma_1} K^*_{Y,\sigma_1} K_{H_2,\sigma_1} C_{H_2} K_{Y,\sigma_1} C_Y}{(1 + K_{Y,\sigma_1} C_Y + K_{E,\sigma_1} C_E + K_{A,\sigma_1} C_A + \sqrt{K_{H_2,\sigma_1} C_{H_2}})^2} \quad (4)$$

$$r_2 = \frac{k_{2,\sigma_1} K^{***}_{Y,\sigma_1} K^{**}_{Y,\sigma_1} K^*_{Y,\sigma_1} K^2_{H_2,\sigma_1} C^2_{H_2} K_{Y,\sigma_1} C_Y}{(1 + K_{Y,\sigma_1} C_Y + K_{E,\sigma_1} C_E + K_{A,\sigma_1} C_A + \sqrt{K_{H_2,\sigma_1} C_{H_2}})^2} \quad (5)$$

$$r_3 = \frac{k_{3,\sigma_2} K^*_{Y,\sigma_2} K_{H_2,\sigma_2} C_{H_2} K_{Y,\sigma_2} C_Y}{(1 + K_{Y,\sigma_2} C_Y + K_{E,\sigma_2} C_E + K_{A,\sigma_2} C_A + \sqrt{K_{H_2,\sigma_2} C_{H_2}})^2} \quad (6)$$

$$r_4 = \frac{k_{4,\sigma_2} K^*_{E,\sigma_2} K_{H_2,\sigma_2} C_{H_2} K_{Y,\sigma_2} C_Y}{(1 + K_{Y,\sigma_2} C_Y + K_{E,\sigma_2} C_E + K_{A,\sigma_2} C_A + \sqrt{K_{H_2,\sigma_2} C_{H_2}})^2} \quad (7)$$

Equations 4−7 can be simplified by partly grouping the constants in the numerator as well as by neglecting the coverage by hydrogen[35] and the alkane. This diminishes the number of degrees of freedom of the system by reducing the number of adjustable parameters:

$$r_1 = \frac{k^*_{1,\sigma_1} K_{Y,\sigma_1} C_Y}{(1 + K_{Y,\sigma_1} C_Y + K_{E,\sigma_1} C_E)^2} \quad (8)$$

$$r_2 = \frac{k^*_{2,\sigma_1} K_{Y,\sigma_1} C_Y}{(1 + K_{Y,\sigma_1} C_Y + K_{E,\sigma_1} C_E)^2} \quad (9)$$

$$r_3 = \frac{k^*_{3,\sigma_2} K_{Y,\sigma_2} C_Y}{(1 + K_{Y,\sigma_2} C_Y + K_{E,\sigma_2} C_E)^2} \quad (10)$$

$$r_4 = \frac{k^*_{4,\sigma_2} K_{E,\sigma_2} C_E}{(1 + K_{Y,\sigma_2} C_Y + K_{E,\sigma_2} C_E)^2} \quad (11)$$

The mass balance for MBY, MBE, and MBA are given by the following equations:

$$\frac{dC_Y}{dt} = \frac{n_{Pd}}{V}(-r_1 - r_2 - r_3) \quad (12)$$

$$\frac{dC_E}{dt} = \frac{n_{Pd}}{V}(r_1 + r_3 - r_4) \quad (13)$$

$$\frac{dC_A}{dt} = \frac{n_{Pd}}{V}(r_2 + r_4) \quad (14)$$

Equations 8−14 were solved simultaneously using Berkeley's Madonna[36] software with Runge−Kutta's method for differential

dx.doi.org/10.1021/ja204557m |J. Am. Chem. Soc. 2011, 133, 12787–12794

equations. Subscripts Y, E, and A refer to the alkyne, alkene, and alkane, respectively. The adsorption constants $K_{Y,\sigma 1}$, $K_{Y,\sigma 2}$, $K_{E,\sigma 1}$, and $K_{E,\sigma 2}$ were set to be equal for all samples since the main premise of the study is that the MBY molecules interact specifically with each type of site, regardless of the size or shape of the nanocrystal. The kinetic constants, however, were varied from sample to sample (Table S2, Supporting Information). The quality of the fitting to the experimental points obtained was satisfactory in all cases, as it can be appreciated in Figure S6 in the Supporting Information.

Since it was observed that activity could be correlated to the relative amounts of plane and edge sites (Table 2), the model was pushed one step further by assuming that the kinetic constants should follow the same principle. They were thus rendered independent of the size and shape of the Pd nanocrystals by expressing them in terms of moles of surface atom of Pd (eq 15).

$$k^{**}_{j,k} = \frac{k^{*}_{j,k}}{D}\left[\frac{\text{mol}}{\text{mol}_{\text{surfPd}}\ \text{s}}\right] \tag{15}$$

where the subscripts j and k correspond to reaction path and site type, respectively, and D refers to the dispersion of the nanocrystal (see Table 1). The constant shown in eq 15 is thus expressed by total amount of surface Pd atoms, but it is not yet specific to one of the two types of sites used in this work. A further normalization with respect to the fraction of each type of site is then necessary:

$$k^{***}_{j,k} = \frac{k^{**}_{j,k}}{x_k}\left[\frac{\text{mol}}{\text{mol}_{\text{surfPd}}\ \text{s}}\right] \tag{16}$$

The constants obtained in this way are specific to a reaction path and active site type, but independent of the size and shape of the nanocrystals. Four specific kinetic constants were estimated and then found to satisfy all samples through eqs 8−16 with errors lower than 20% (see Table 3). These values suggest that plane sites are 3.5 times more active in the selective hydrogenation of MBY to MBE, but that this reaction can indeed take place over the edge sites as well. Furthermore, it can be seen that the consecutive hydrogenation of MBE to MBA on edge sites is kinetically favored.

The kinetics obtained for all samples were successfully modeled using this set of constants. It can be seen (Figure 4) that the fitting remains accurate despite the experimental errors and the simplifications made. The conjugation of eqs 8−16 with the set of empirically obtained constants (Table 3) provides a powerful tool that allows for a full kinetic description of a Pd nanocrystal regardless of its size and shape, as long as the statistics of the surface atoms can be estimated.

Optimization of Size and Shape for the Pd Nanocrystals. Size and shape optimization is often performed by considering only *activity* as the optimization criterion.[34] If this approach is applied, then eq 3 can be combined with the statistics of surface for common nanocrystal shapes to yield the graph presented in

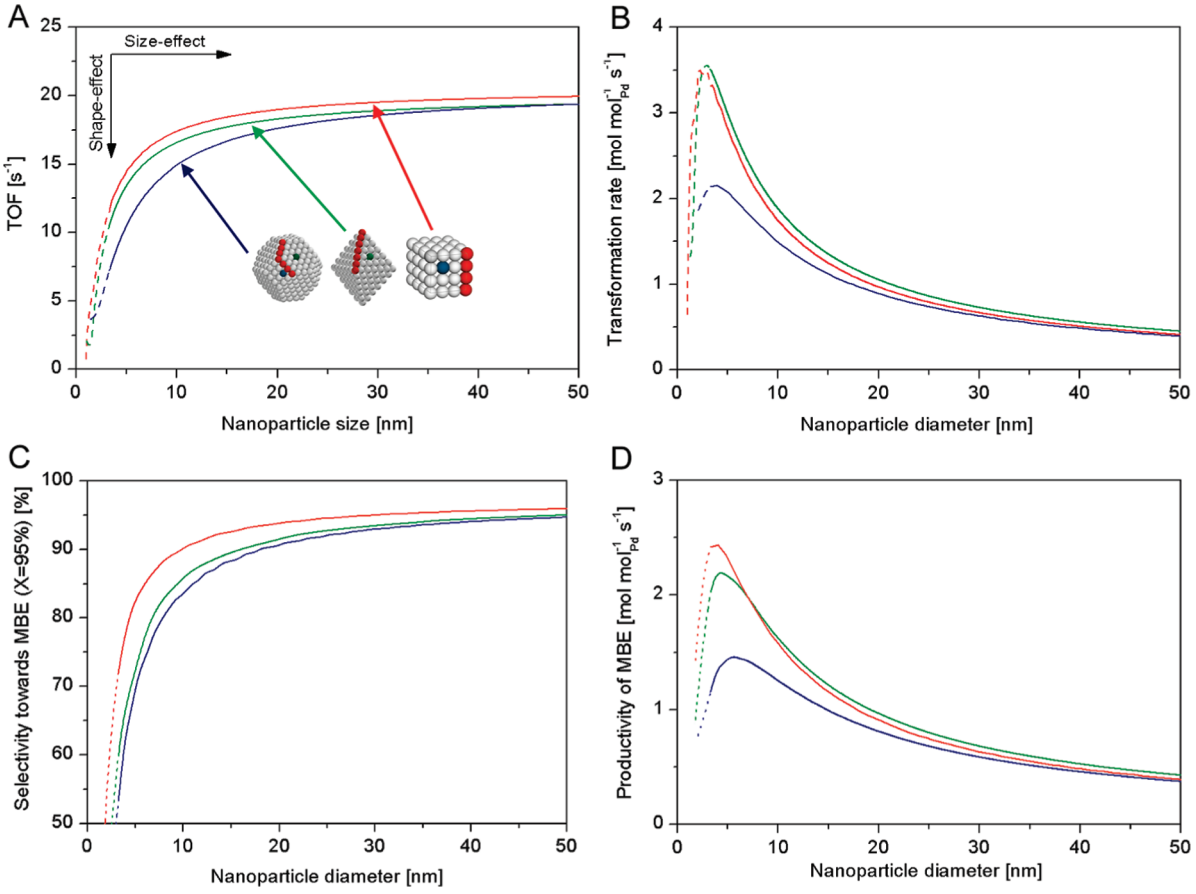

Figure 5. Optimization of Pd nanocrystal size and shape based on (A) TOF, (B) MBY transformation rate, (C) selectivity toward 2-methyl-3-buten-2-ol (MBE) at 95% conversion, and (D) transformation rate, or productivity, of MBE.

Figure 5A. As expected, *shape* does not exert a considerable effect on TOF for MBY transformation since both (111) and (100) planes behave similarly. Cubo-octahedra, however, are slightly disfavored due to the larger fraction of edge atoms (or σ_2 sites), which are considerably less active in the hydrogenation of MBY relative to plane atoms (or σ_1 sites). The most significant *size effect* is observed in the 3−20 nm range, after which the reaction becomes size and shape independent with respect to TOF. Nanocrystals smaller than 3 nm in size start to lose their bulk properties,[2,25] and, consequently, the catalytic behavior may not follow the prediction. This region is depicted with dotted lines.

If, on the other hand, the MBY transformation rate is referenced to the total amount of Pd, then both size and shape effects change substantially (Figure 5B). While there would be no difference between cubic or octahedral nanocrystals, cuboctahedra will be significantly less active due to their low dispersions. This difference, however, can be neglected for particles larger than 15 nm in size, after which the reaction becomes again size and shape independent. Therefore, if the activity of a catalyst is used as the only optimization criterion, either cubes or octahedra of roughly ∼5 nm in size should be the best choice for the catalyst.

Selectivity is a very, if not the most, important catalytic property for most applications. Therefore, a dual *selectivity−activity criterion* for optimization seems to be well-justified. To achieve this, we had to combine eqs 8−16 with the set of empirically obtained constants (Table 3) and the statistics of surface atoms for the nanocrystals in study. This allowed us to obtain simulation curves analogous to those shown in Figures S6 and 4 for cubic, octahedral, and cuboctahedral nanocrystals with sizes in the range 3−50 nm (Figure S7, Supporting Information). From such simulations, the selectivity toward MBE at 95% conversion can be estimated for all different nanocrystals:

$$S_E = \frac{C_E}{C_Y^0 - C_Y} \qquad (17)$$

Figure 5C shows the results of the simulations. Selectivity toward MBE increases monotonically with particle size in the order cubes > octahedra > cuboctahedra. Figure 5B and C can be combined (Figure 5D) to simultaneously optimize selectivity and activity, showing that the reaction is indeed structure sensitive in the size range studied. In this case, the productivity of the target product is plotted against particle size for all three shapes. As a result, two optimal nanocrystals can be proposed. If the productivity of MBE is to be maximized, then cubic nanocrystals of approximately 3−5 nm would be the best choice. If, on the other hand, a pure selectivity criterion is judged as more appropriate, then larger cubic nanocrystals should be chosen. In this case, a compromise between productivity and selectivity must be reached.

The structure sensitivity of a chemical reaction is specific for each catalytic system.[25] Therefore, such a modeling-simulation approach combined with the experimental kinetic data obtained from uniform, well-defined metal nanocrystals gives a powerful tool for rational catalyst design for a given chemical reaction.

CONCLUSIONS

We have studied the structure sensitivity of the water-assisted selective hydrogenation of MBY over uniform, unsupported Pd nanocrystals with different sizes and shapes. The Pd nanocrystals were prepared with cubic, octahedral, and cuboctahedral shapes using a solution-phase method, with PVP serving as a stabilizing agent. The observed activity and selectivity suggested that two types of active sites were involved in the catalysis, which differ in coordination numbers and are located on planes and edges, respectively. A two-site Langmuir−Hinshelwood kinetic model allowed for an accurate description of the experimentally observed activity and selectivity. Semihydrogenation to MBE was found to occur on both types of sites, but the reactivity depended on the coordination number of the atoms. Edge atoms were 4-fold less active in the semihydrogenation as compared to the plane atoms. Overhydrogenation to MBA occurred solely on the edge atoms presumably due to increased adsorption strength of the alkene. Selectivity was then linked to the fraction of edge sites on each type of nanocrystal. Kinetic simulations pointed toward ∼3−5 nm cubic nanocrystals as an optimal catalyst for the highest productivity of MBE.

Metal nanocrystals with tuned sizes and shapes prepared via colloidal techniques can be considered as a *new generation of model catalysts*, which allow overcoming the material and pressure gaps in catalysis and complementing single-crystal studies, which inherently lack the complexity of industrial catalysis. The approach shown in this work provides a powerful tool for rational catalyst design for industrially relevant chemical reactions under real conditions.

ASSOCIATED CONTENT

Supporting Information. Statistics of surface atoms for common fcc crystal shapes, HRTEM imaging and particle size distribution of the nanocrystals, XPS spectra of CUB6 sample, TEM image of cubic nanoparticles after the reaction, complete Langmuir−Hinshelwood mechanism for the hydrogenation of 2-methyl-3-butyn-2-ol, kinetic modeling with one set of adsorption constants, and kinetic simulation results to estimate the productivity of the target product MBE. This material is available free of charge via the Internet at http://pubs.acs.org.

AUTHOR INFORMATION

Corresponding Author
lioubov.kiwi-minsker@epfl.ch

ACKNOWLEDGMENT

This work was supported by the Swiss National Science Foundation (grant no. 200021-118067 to L.K.M.) and the U.S. National Science Foundation (DMR-0804088 to Y.X.). The authors thank Marco Cantoni (EPFL-SB-CIME) for the high-resolution TEM images and Nicolas Xanthopoulos (EPFL-SB-CIME) for the XPS measurements.

REFERENCES

(1) Boudart, M. *Chem. Rev.* **1995**, *95*, 661.
(2) Che, M.; Bennett, C. O. *Adv. Catal.* **1989**, *36*, 55.
(3) Molnar, A.; Sarkany, A.; Varga, M. *J. Mol. Catal. A* **2001**, *173*, 185.
(4) Van Hardeveld, R.; Hartog, F. *Surf. Sci.* **1969**, *15*, 189.
(5) Freund, H. J. *Top. Catal.* **2008**, *48*, 137.
(6) Silvestre-Albero, J.; Rupprechter, G.; Freund, H. J. *J. Catal.* **2006**, *240*, 58.
(7) Silvestre-Albero, J.; Rupprechter, G.; Freund, H. J. *Chem. Commun.* **2006**, *1*, 80.

(8) Sasaki, M.; Osada, M.; Higashimoto, N.; Yamamoto, T.; Fukuoka, A.; Ichikawa, M. *J. Mol. Catal. A* **1999**, *141*, 223.
(9) Balint, I.; Miyazaki, A.; Aika, K. *Phys. Chem. Chem. Phys.* **2004**, *6*, 2000.
(10) Narayanan, R.; El-Sayed, M. A. *Nano Lett.* **2004**, *4*, 1343.
(11) Narayanan, R.; El-Sayed, M. A. *J. Phys. Chem. B* **2004**, *108*, 5726.
(12) Bratlie, K. M.; Lee, H.; Komvopoulos, K.; Yang, P. D.; Somorjai, G. A. *Nano Lett.* **2007**, *7*, 3097.
(13) Habas, S. E.; Lee, H.; Radmilovic, V.; Somorjai, G. A.; Yang, P. *Nat. Mater.* **2007**, *6*, 692.
(14) Semagina, N.; Kiwi-Minsker, L. *Catal. Rev.* **2009**, *51*, 147.
(15) Tao, A. R.; Habas, S.; Yang, P. D. *Small* **2008**, *4*, 310.
(16) Xia, Y.; Xiong, Y. J.; Lim, B.; Skrabalak, S. E. *Angew. Chem., Int. Ed.* **2009**, *48*, 60.
(17) Jia, C. J.; Schuth, F. *Phys. Chem. Chem. Phys.* **2011**, *13*, 2457.
(18) Boitiaux, J. P.; Cosyns, J.; Robert, E. *Appl. Catal.* **1987**, *32*, 145.
(19) Le Bars, J.; Specht, U.; Bradley, J. S.; Blackmond, D. G. *Langmuir* **1999**, *15*, 7621.
(20) Li, Y.; Boone, E.; El-Sayed, M. A. *Langmuir* **2002**, *18*, 4921.
(21) Semagina, N.; Kiwi-Minsker, L. *Catal. Lett.* **2009**, *127*, 334.
(22) Semagina, N.; Renken, A.; Laub, D.; Kiwi-Minsker, L. J. *J. Catal.* **2007**, *246*, 308.
(23) Bhattacharjee, S.; Dotzauer, D. M.; Bruening, M. L. *J. Am. Chem. Soc.* **2009**, *131*, 3601.
(24) Wilson, O. M.; Knecht, M. R.; Garcia-Martinez, J. C.; Crooks, R. M. *J. Am. Chem. Soc.* **2006**, *128*, 4510.
(25) Bond, G. C. *Chem. Soc. Rev.* **1991**, *20*, 441.
(26) Lim, B.; Jiang, M. J.; Tao, J.; Camargo, P. H. C.; Zhu, Y. M.; Xia, Y. N. *Adv. Funct. Mater.* **2009**, *19*, 189.
(27) Jin, M.; Liu, H.; Zhang, H.; Xie, Z.; Liu, J.; Xia, Y. *Nano Res.* **2011**, *4*, 83.
(28) Piccolo, L.; Valcarcel, A.; Bausach, M.; Thomazeau, C.; Uziob, D.; Berhault, G. *Phys. Chem. Chem. Phys.* **2008**, *10*, 5504.
(29) Quintanilla, A.; Butselaar-Orthlieb, V. C. L.; Kwakernaak, C.; Sloof, W. G.; Kreutzer, M. T.; Kapteijn, F. *J. Catal.* **2010**, *271*, 104.
(30) Crespo-Quesada, M.; Grasemann, M.; Semagina, N.; Renken, A.; Kiwi-Minsker, L. *Catal. Today* **2009**, *147*, 247.
(31) Semagina, N.; Grasemann, M.; Xanthopoulos, N.; Renken, A.; Kiwi-Minsker, L. *J. Catal.* **2007**, *251*, 213.
(32) Boitiaux, J. P.; Cosyns, J.; Vasudevan, S. *Appl. Catal.* **1983**, *6*, 41.
(33) Hub, S.; Hilaire, L.; Touroude, R. *Appl. Catal.* **1988**, *36*, 307.
(34) Ma, R.; Semagina, N. *J. Phys. Chem. C* **2010**, *114*, 15417.
(35) Singh, U. K.; Albert Vannice, M. *J. Catal.* **2000**, *191*, 165.
(36) Macey, R. I.; Oster, G. F. *Berkeley MadonnaTM*; 1997.